

LARLUS: Laparoscopic Augmented Reality from Laparoscopic Ultrasound

Mohammad Mahdi Kalantari^{1*}, Erol Ozgur¹,
Mohammad Alkhatib¹, Emmanuel Buc², Bertrand Le Roy³,
Richard Modrzejewski⁴, Youcef Mezouar¹, Adrien Bartoli^{2, 4}

¹Clermont Auvergne INP, Institut Pascal, Clermont-Ferrand, France.

²University Hospital of Clermont-Ferrand, France.

³University Hospital of Saint-Etienne, France.

⁴SURGAR, 22 allée Alan Turing, Clermont-Ferrand, France.

*Corresponding author E-mail:
mohammad.mahdi.kalantari@sigma-clermont.fr;

Abstract

Purpose. This research endeavors to improve tumor localization in minimally invasive surgeries (MIS), a challenging task primarily attributable to the absence of tactile feedback and limited visibility. The conventional solution uses laparoscopic ultrasound (LUS) which has a long learning curve and is operator-dependent.

Methods. The proposed approach involves augmenting LUS images onto laparoscopic images to improve the surgeon's ability to estimate tumor and internal organ anatomy. This augmentation relies on LUS pose estimation and filtering.

Results. Experiments conducted with clinical data exhibit successful outcomes in both the registration and augmentation of LUS images onto laparoscopic images. Additionally, noteworthy results are observed in filtering, leading to reduced flickering in augmentations.

Conclusion. The outcomes reveal promising results, suggesting the potential of LUS augmentation in surgical images to assist surgeons and serve as a training tool. We have used the LUS probe's shaft to disambiguate the rotational symmetry. However, in the long run, it would be desirable to find more convenient solutions.

Keywords: Minimally invasive surgery, Tumor localization, Laparoscopic ultrasound, Augmented reality

1 Introduction

Minimally invasive surgery (MIS) has numerous benefits to the patients compared to open surgery. However, MIS does not allow a surgeon to palpate an organ which in turn complicates tumor localization. Laparoscopic ultrasonography (LUS) is used to address this downside. Nonetheless, LUS also has its own drawbacks. It requires a long learning curve and an expert surgeon for maneuvering the LUS probe. We can thus expect that an augmented reality (AR) solution offers significant assistance to surgeons by simplifying the use of LUS. Such an AR solution should be able to work under default operating room (OR) conditions (*i.e.*, without additional sensors and markers) so that it is practical. It should also run in real-time and not require any initialization so that the surgical workflow is not disrupted.

State-of-the-art methods for tumor localization in MIS are not able to form a practical and disruptionless solution. They use either additional sensors [1], markers, or fiducials [1, 2], require initialization, or do not work in real time [3]. In contrast, we propose a practical and disruptionless AR solution.

2 Methods

We first model the LUS probe and present its geometry. Next, we introduce our AR solution. It relies on several key components including single-shot pose estimation, filtering, and augmentation. These components are explained briefly in the subsequent sections.

2.1 LUS Probe Modeling and Geometry

We model the LUS probe geometry as in figure 1. The LUS probe has two levers l_1 and l_2 on the shaft's distal end to pivot the head, which is not shown in figure 1. Lever l_1 rotates the head up and down and lever l_2 rotates the head left and right with respect to the shaft. In figure 1, $\{\underline{x}, \underline{y}, \underline{z}\}$ denote the axes and \mathbf{o} the origin of the camera coordinate frame, \mathbf{t} denotes the tip position (*i.e.*, hemisphere center) and the unit vector \underline{h} represents the LUS probe's head axis direction. Similarly, the unit vector \underline{s} represents the LUS probe's shaft axis direction. The vector $\underline{h} \times \underline{s}$ forms the normal of the LUS image plane (*i.e.*, the blue plane) when the head's lateral movement lever is left constant. The vector \underline{m} represents the normal of the interpretation plane defined by head axis line l_h and \mathbf{o} . The vector \underline{n} represents the normal of the interpretation plane defined by shaft axis line l_s and \mathbf{o} . The rotation angle α around \underline{m} quantifies the depth variation of the LUS probe's head axis direction \underline{h} on its interpretation plane. Similarly, the rotation angle β around \underline{n} quantifies the depth variation of the LUS probe's shaft axis direction \underline{s} on its interpretation plane. Finally, the rotation angle θ quantifies the LUS probe's head rotation around its axis direction \underline{h} .

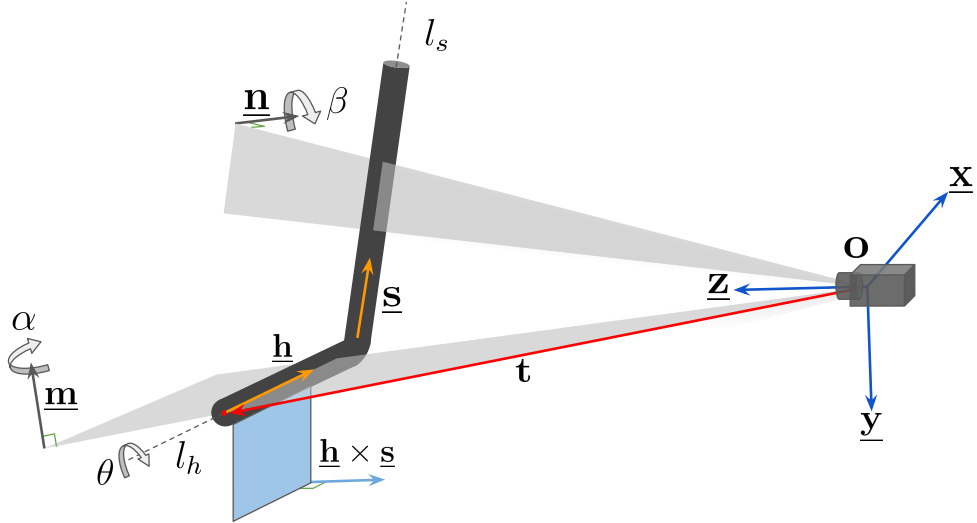


Fig. 1 LUS probe geometry and modeling. The mathematical notation is explained in the main text.

2.2 Augmented Reality Solution

Requirement

The proposed AR solution requires 6 DoF LUS pose estimation. However, we can only estimate 5 DoF poses from the LUS head's spherocylinder shape. The 6th DoF cannot be observed directly because of the rotational symmetry around the LUS head's axis. Therefore, we assume the following to meet this requirement.

Assumption

We assume that LUS lever l_2 is kept intact so that no lateral head rotation happens with respect to the shaft. This assumption implies by construction that the LUS imaging plane $\Pi_{\underline{L}}$, shown in blue in figure 1, remains inside the plane Π_L defined by the shaft axis line l_s and head axis line l_h . This is a mild assumption and it can be easily satisfied by informing the surgeon not to use lever l_2 when they maneuver the LUS probe.

Algorithm

The proposed AR solution's pseudo implementation is given in algorithm 1. We call it LARLUS (Laparoscopic Augmented Reality from Laparoscopic Ultrasound).

In algorithm 1, line 1 initializes the pose tensor using zeros vector $\mathbf{0}_{6 \times 1}$ with a history of 1. Line 2 initializes the pose covariance tensor using a 6×6 identity matrix scaled by infinite uncertainty $\text{diag}(\infty)_{6 \times 6}$ with a history of 1. Line 3 starts the main loop. Line 4 grabs synchronously the laparoscopic image \mathbf{I}_{LAP} and the LUS image \mathbf{I}_{LUS} . Line 5 estimates the LUS pose ξ and also returns the number of measured degrees of freedom given the laparoscope's camera intrinsic calibration matrix \mathbf{K} , the laparoscope image \mathbf{I}_{LAP} , and the LUS probe's spherocylinder radius r . Line 5 uses

Algorithm 1: LARLUS

```

1  $\xi_{\square} \leftarrow \mathbf{0}_{6 \times 1 \times 1}$  // Initialize LUS pose history tensor
2  $\Sigma_{\square} \leftarrow \text{diag}(\infty)_{6 \times 6 \times 1}$  // Initialize pose covariance history tensor
3 while not exit do
4    $\{\mathbf{I}_{LAP}, \mathbf{I}_{LUS}\} \leftarrow \text{grab\_images}()$  // Read laparoscope and LUS images
5    $\{\xi, n_{dof}\} \leftarrow \text{LUP}^*(\mathbf{K}, \mathbf{I}_{LAP}, r)$  // Single-shot pose estimation
6    $\{\hat{\xi}, \hat{\Sigma}\} \leftarrow \text{filtering\_on\_depth\_variations}(\xi_{\square}, \Sigma_{\square}, \xi, n_{dof})$ 
7   if  $\text{norm}(\hat{\Sigma}) < \tau$  then  $\text{display}(\text{augment}(\mathbf{I}_{LAP}, \mathbf{I}_{LUS}))$  else  $\text{display}(\mathbf{I}_{LAP})$ 
8    $\xi_{\square} \leftarrow \xi_{\square}.\text{add}(\hat{\xi}), \Sigma_{\square} \leftarrow \Sigma_{\square}.\text{add}(\hat{\Sigma})$  // Stack into the tensors
9 end

```

the LUP* algorithm, which is an improved version of our previous LUP algorithm [4]. Line 6 filters temporally the quadruplets $\{\alpha, \beta, \theta, \|\mathbf{t}\|\}$ illustrated in figure 1. The quadruplets are formed by decoupling the pose history. Relative rotation angles α , β , and θ are computed from two consecutive frames. The quadruplets encode the depth variations which are also the most sensitive parts of the pose estimation. Once the filtered quadruplets are available, they are used to compute the updated LUS pose $\hat{\xi}$ and covariance $\hat{\Sigma}$. Line 7 augments the laparoscopic image \mathbf{I}_{LAP} with the LUS image \mathbf{I}_{LUS} , if the pose uncertainty norm-2 remains below a threshold value τ . Line 8 stacks the updated LUS pose and its covariance in the history tensors for the next filtering step. Line 9 ends the main loop.

2.2.1 Single-shot Pose Estimation

LUP* represents an improved version of LUP [4] (Laparoscopic Ultrasound Pose), which inherits all the advantages of LUP, namely, being free from markers, from extra sensors beyond the surgical camera, and from the need for (re)initialization, and being able to run in real-time. The improvements are as follows.

(i) LUP* is twice faster than LUP. This owes to two factors. First, LUP* uses the Hough transform to construct line samples for RANSAC. This yields substantially fewer samples to test compared to the random point sampling for the line construction in LUP. Second, LUP* forms clusters on the contour points not belonging to the lines' best consensus sets, prior to choosing the cluster that includes the contour points related to only the hemisphere silhouette of the LUS probe's tip. This is achieved by checking the symmetry of clusters with respect to the LUS probe's head axis, eliminating many false contour points.

(ii) LUP* is more robust than LUP to hard cases. This owes to the second improvement described directly above: eliminating clusters' points that are not part of the hemisphere silhouette of the LUS probe's tip makes the pose estimation more robust.

(iii) LUP* is more integrated than LUP, as it directly provides the 6 DoF pose estimate when the LUS shaft is visible, whereas LUP provides only 5 DoF and would require an extra processing step to complete the pose.

2.2.2 Filtering on Depth Variations

We study the LUS probe's geometry to define the most suitable variables for filtering. This is for two reasons. First, we want to filter only the most noise-sensitive parts of the pose estimates. Second, we want to avoid over-filtering on the pose estimates because of the possible couplings between the variables. Consequently, we ended up forming the quadruplets $\{\alpha, \beta, \theta, \|t\|\}$ given in section 2.1. We consider that they are well decoupled from each other. The variable $\|t\|$ is an absolute value and is estimated at each single frame. The variables $\{\alpha, \beta, \theta\}$ are incremental values and are estimated as differences from two consecutive frames. $\{\alpha, \beta, \theta\}$ are expressed within the coordinate system of the subsequent frame. We filtered each variable using a 1D Unscented Kalman Filter (UKF) with a constant velocity motion model and white noise for the measurements and the motion model.

2.2.3 Augmented Reality Rendering

Augmentation requires implementing two components: *(i)* homography computation between the LUS image and the laparoscopic image; and *(ii)* blending of the warped LUS image with the laparoscopic image.

Homography computation

Homography computation requires establishing at least four corresponding points between I_{LUS} and I_{LAP} . We stipulate those four points as the corners of the LUS probe's image plane. We first compute these four points in the laparoscope coordinate frame as follows. The first point, the top-left corner, is positioned at a predetermined location relative to the LUS probe's tip (*i.e.*, the hemisphere center). Once the image plane's top-left corner point is located on the LUS probe (*e.g.*, using either calibration, or LUS probe's CAD model, or direct measurement), the remaining corner points are straightforward to compute, given the estimated LUS probe's pose and the LUS image plane's width and height read from the LUS' machine settings. We then project these four points onto the laparoscopic image to form the corresponding pairs of points. These four pairs of points are used to compute the homography mapping.

Blending

We blend the LUS image and the laparoscopic image in five steps. First, the gray-scale LUS image is converted to a green-scale LUS image to enhance visibility. Second, the transparency of the green-scale LUS image as we get closer to the edges is increased linearly. Third, the green-scale LUS image from the second step is warped using the homography mapping. Fourth, the warped green-scale LUS image is blended with the laparoscopic image as a linear combination of both. Fifth, the segmented LUS probe from the laparoscopic image, using the mask generated from the segmentation network, is overlaid over the blended image as the LUS probe's head should occlude the augmented LUS image.

3 Experimental Results and Discussion

We first present experimental results on single-shot pose estimation, filtering, and augmentation using laparoscopic liver surgery images. We then discuss the results.

The main dataset used in all of the experiments is a sequence of 144 images. It is played 4 times, namely twice forward and backward, to form a longer continuous sequence of $144 \times 4 = 576$ images. In addition, there is another sequence of 120 images from another surgery used in section 3.1.

3.1 Single-shot Pose Estimation Results

We performed 5 DoF pose estimations on a dataset with LUP and LUP*. The average time required to estimate pose from the unclassified contour points is 15 ms with 3 ms std for LUP*, while it is 35 ms with 10 ms std for LUP. The large differences in the mean and standard deviation confirm the theoretical speed improvement brought by LUP*. LUP* is also more robust against the failure cases of LUP: it resolves 100% of the failure cases of LUP in the first dataset (3 out of 3 from the total of 144 frames) and 20% of the failure cases of the second dataset (1 out of 5 from the total of 120 frames). We illustrate such a case in figure 2. As one can observe, LUP* succeeds in estimating a proper pose while LUP fails. Finally, the ability of LUP* to estimate 6 DoF pose in the presence of the LUS shaft is demonstrated in the ensuing experiments.

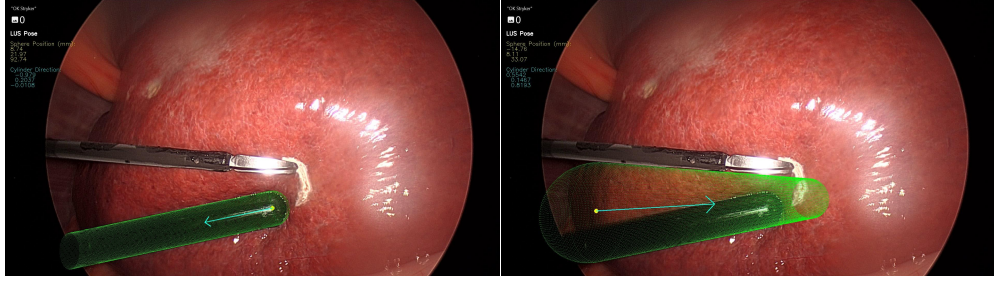


Fig. 2 LUP* pose estimation (on the left) versus LUP pose estimation (on the right).

3.2 Filtering Results

We compare in figure 4 the filtered and unfiltered depth-related variables used in pose estimations. We can observe that the filtered variables are less noisy, which in return improves the augmentations by reducing flickering, as demonstrated in figure 3. Subsequently, this reduces surgeon's eyes fatigue.

3.3 Augmentation Results

We demonstrate LARLUS in figure 5. It shows three augmentation instances of LUS images (green semi-transparent planes) on the laparoscopic liver images. The augmentations aim to help surgeons localize tumors.

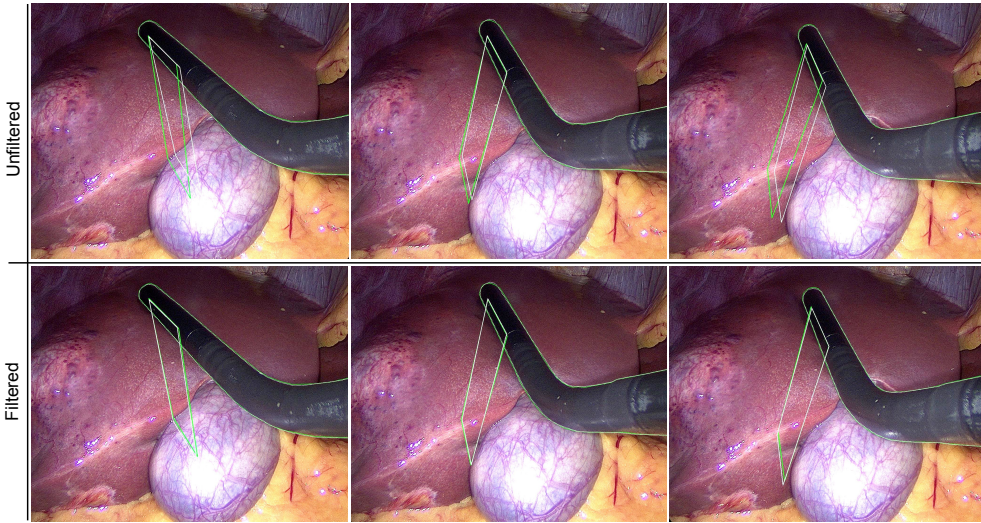


Fig. 3 The upper row shows the LUS imaging planes without filtering. The lower row shows the LUS imaging planes with filtering. In each frame, the green contour denotes a current configuration at an instant k , while the white contour denotes the previous configuration at the instant $k - 1$. One can observe that, without filtering, even a slight LUS probe movement might flicker the LUS imaging plane considerably because of sensitivity to noise.

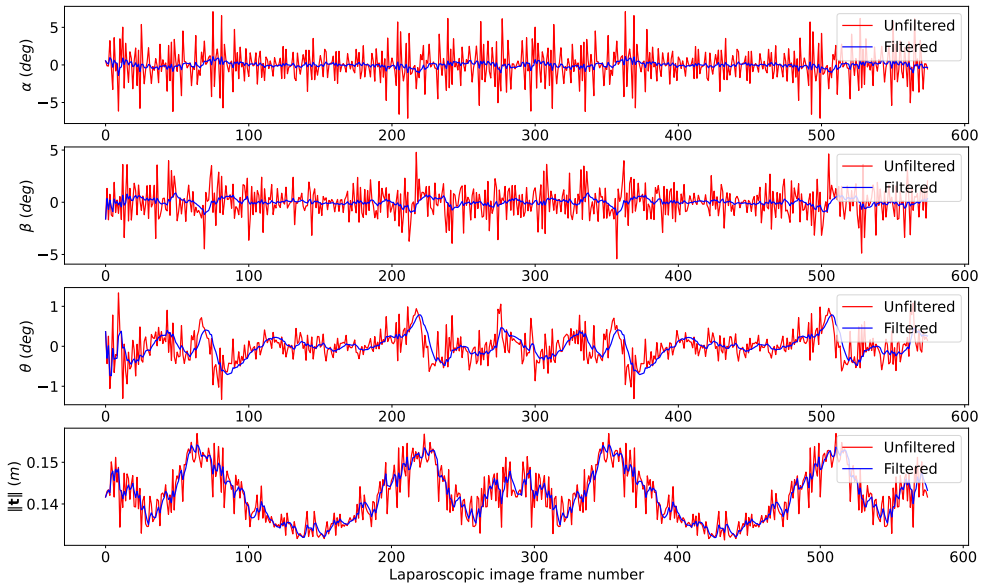


Fig. 4 Unfiltered and filtered depth-related variables.



Fig. 5 Multiple augmentation instances from LARLUS.

3.4 Discussion

We discuss the sensitivity to noise and the limitations of the proposed method.

3.4.1 On Sensitivity to Noise

Depth-related estimates like the quadruplet $\{\alpha, \beta, \theta, \|\mathbf{t}\|\}$ are about an order of magnitude more sensitive to the image contour segmentation errors than lateral estimates. This is because the ratio of the LUS probe's head distance to the laparoscope (*i.e.*, about 10 cm) over the LUS' radius (*i.e.*, about 0.5 cm) is usually high. This ratio forms an amplification factor on depth errors. Subsequently, this generates flickering on the augmentations. In short, the better the image contour segmentation, the more accurate the depth-related estimates. Until a better segmentation method is proposed, we improve the augmentations by filtering the depth-related variables that are decoupled from each other as much as possible.

3.4.2 On Limitations

LUS shaft visibility

The primary limitation is that LARLUS requires the LUS shaft to be visible during tumor localization to resolve the 6th pose DoF, which is not always feasible.

Possible solutions

LUS shaft visibility requirement can be mitigated by one or several of the following leads:

- *Solutions with user notification.* When the covariance of the lost 6th DoF exceeds an upper bound, the AR software could use text, sound, or graphics to prompt the surgeon for the need to show the LUS shaft in order to restore AR. This would allow the covariance to decrease below the upper bound and to re-estimate the lost 6th DoF with acceptable accuracy.
- *Solutions with robotics surgery.* A first solution could be to visually servo the robot to control the camera so that the LUS probe's shaft is kept in the field of view. A second solution could be, when the LUS probe is also maneuvered by a robot, to read the forward kinematics from the robots and use the known relative pose between their base coordinate frames.
- *Solutions from computer vision.* A first solution could be to estimate the LUS probe's keyhole position on the patient's abdomen [5]. Knowing the LUS probe's 5 DoF

head pose and the LUS probe’s head length, we could then retrieve the 6th DoF by first computing the intersection point between the head and the shaft, and then the shaft direction vector from the intersection point’s position and the keyhole position. The second solution could be to register the preoperative organ 3D model to the intraoperative LUS image [6]. Assuming that the probe’s tip is in contact with the organ would then provide an extra constraint to resolve the 6th pose DoF.

4 Conclusion and Future Work

Based on the experimental results and measurements, as well as on direct feedback from surgeons, **LARLUS** is deemed to provide promising results. It shows that LUS augmentation in the surgical image may assist in localizing tumors and training inexperienced surgeons.

We give two main leads for future work. First, we shall improve the LUS probe segmentation in the laparoscopic images in **LUP***. Second, we shall improve **LARLUS** to reconstruct the 3D tumor volume from the segmented LUS images and augment it on the laparoscopic images in real-time. For that, because the intraoperative LUS images are usually very noisy and present artifacts, we shall also consider integrating the preoperative 3D tumor model into the problem to form a coupled registration-reconstruction solution for the augmentations.

5 Compliance with Ethical Standards

Mohammad Mahdi Kalantari declares to have no potential conflicts of interest. Erol Ozgur declares to have no potential conflicts of interest. Mohammad Alkhatib declares to have no potential conflicts of interest. Emmanuel Buc declares to have no potential conflicts of interest. Bertrand Le Roy declares to have no potential conflicts of interest. Richard Modrzejewski declares to have no potential conflicts of interest. Youcef Mezouar declares to have no potential conflicts of interest. Adrien Bartoli declares to have no potential conflicts of interest.

All procedures involving human participants were in accordance with the ethical standards of the institutional and/or national research committee and with the 1964 Helsinki Declaration and its later amendments or comparable ethical standards. This study is also supported by ethical approval with ID IRB00008526-2019-CE58 issued by CPP Sud-Est VI in Clermont-Ferrand, France.

Informed consent was obtained from the patients included in the study.

Acknowledgement

This work is funded by project ANR JCJC - IMMORTALLS.

References

- [1] Pelanis, E., Teatini, A., Eigl, B., Regensburger, A., Alzaga, A., Kumar, R.P., Rudolph, T., Aghayan, D.L., Riediger, C., Kvarnström, N., Elle, O.J., Edwin, B.: Evaluation of a novel navigation platform for laparoscopic liver surgery with organ deformation compensation using injected fiducials. *Medical Image Analysis* **69**, 101946 (2021)
- [2] Rabbani, N., Calvet, L., Espinel, Y., Le Roy, B., Ribeiro, M., Buc, A., Bartoli, A.: A methodology and clinical dataset with ground-truth to evaluate registration accuracy quantitatively in computer-assisted laparoscopic liver resection. *Computer Methods in Biomechanics and Biomedical Engineering: Imaging & Visualization* **10**(4), 441–450 (2022)
- [3] Espinel, Y., Ozgur, E., Calvet, L., Le Roy, B., Buc, E., Bartoli, A.: Combining visual cues with interactions for 3d–2d registration in liver laparoscopy. *Annals of Biomedical Engineering* **48**(6), 1712–1727 (2020)
- [4] Kalantari, M.M., Ozgur, E., Alkhatib, M., Buc, E., Le Roy, B., Modrzejewski, R., Mezouar, Y., Bartoli, A.: Markerless ultrasound probe pose estimation in minimally invasive surgery. *IEEE International Conference on Robotics and Automation, ICRA* (2024)
- [5] Ribeiro, M., Espinel, Y., Rabbani, N., Pereira, B., Bartoli, A., Buc, E.: Augmented reality guided laparoscopic liver resection: A phantom study with intraparenchymal tumors. *Journal of Surgical Research* (2024) <https://doi.org/10.1016/j.jss.2023.12.014>
- [6] Montaña-Brown, N., Ramalhinho, J., Allam, M., Davidson, B., Hu, Y., Clarkson, M.J.: Vessel segmentation for automatic registration of untracked laparoscopic ultrasound to ct of the liver. *Int J Comput Assist Radiol Surg* (2021) <https://doi.org/10.1007/s11548-021-02400-6>